Electrochemical Stability of n-Si Photoanodes Protected by TiO2 Thin Layers Grown by Atomic Layer Deposition

Maxime E Dufond, Jean-Noël Chazalviel, Lionel Santinacci

Journal of The Electrochemical Society, 2021 **168** 031509

Electrochemical Stability of n-Si Photoanodes Protected by TiO_2 Thin Layers Grown by Atomic Layer Deposition

Maxime E. Dufond,[1] Jean-Noël Chazalviel,[2,a] and Lionel Santinacci[1,z]

[1]*Aix-Marseille Univ., CNRS, CINaM, Marseille, France*
[2]*Physique de la Matière Condensée, CNRS-Ecole Polytechnique, 91128 Palaiseau, France*

This work investigates the n-Si photoanodes corrosion protection by Atomic Layer Deposition (ALD) of a TiO_2 film. A specific electrochemical experimental sequence (including successive rest potential measurements and voltammetries under illumination or not) has been established to study the stability of the electrodes in KOH. Depending on the deposition conditions (precursor composition and temperature), the electrochemical properties of the layers are different. The photoanodes coated using titanium tetraisopropoxide (TTIP) at low temperature exhibit a low photocurrent (j_{ph}) that is progressively enhanced during the electrochemical sequence and their stability decreases. When using tetrakis(dimethylamido)titanium (TDMAT), the j_{ph} is almost constant and the film prevents from corrosion. The characterizations show that the ALD parameters drive the microstructure of the layer that is found critical for the electrochemical response. A hydrogen doping occurring during the open circuit potential measurements under illumination is evidenced by IR spectroscopy. It is mainly localized at the grain boundaries and pores of the layers as well as in the n-Si and it modifies the charge transfer at the electrode/solution junction and the hydrogen diffusion weakens the film causing the Si corrosion. The different charge transfer mechanisms are finally proposed depending on the ALD conditions and the film thickness.

 [DOI: 10.1149/1945-7111/abeaf3]

Manuscript submitted January 5, 2021; revised manuscript received February 25, 2021. Published March 10, 2021. *This paper is part of the JES Focus Issue on Characterization of Corrosion Processes in Honor of Philippe Marcus.*

Supplementary material for this article is available online

Renewable energy sources such as sun and wind are promising but their use is limited by their intermittent nature. Since the pioneering work of Fujishima and Honda,[1] hydrogen and other solar fuels appeared as encouraging paths to store and transport renewable energy. However, water photoelectrolysis technology requires significant improvements prior to be commercialized.[2–4] Among the various possible ways of investigations, the choice of a cost-effective absorber is critical. Silicon could be a good candidate because this abundant semiconductor absorbs most of the visible light ($E_g^{Si} = 1.12$ eV)[5,6] and it can easily be structured by various porous etching approaches.[7] It exhibits, however, several drawbacks such as an indirect bandgap, a non optimized position of the band edges with respect to the redox potential of water, a slow kinetics regarding the photoelectrolysis, and as many semiconductors,[8] it corrodes easily in KOH which is an electrolyte often used in photoelectrochemical cells.[5] In the 1980s, several attempts have been tried to address this limitation by forming protective films such as ITO, Fe_2O_3, Mn_2O_3, Pt-doped SiO_2 using ion beam sputtering, electron beam deposition, precipitation or anodization, respectively.[9–12] More recently, physical vapor deposition (PVD) and atomic layer deposition (ALD) have been successfully used to grow thin protective layers of TiO_2, Fe_2O_3 or MnO_2.[13–16] An exhaustive review reports on the different thin film approaches for the protection of semiconducting photoelectrodes.[17] The semiconductive oxides are often selected because they are stable in KOH but TiO_2 has attracted the largest attention (see e.g. Refs. 14, 18–24). In addition to preventing the electrode corrosion, a synergy is envisioned between Si and TiO_2. Electron/hole pair photogenerations are expected in the wide bandgap semiconductor ($E_g^{TiO_2} \approx 3.2$ eV) under UV illumination while photocarriers are expected in the Si for deeper penetrating light and longer wavelengths.

ALD is well-suited for this goal because it generates homogeneous coatings on planar and tortuous substrates with a near perfect control of both thickness and chemical composition. It is usually carried out in the gas phase but recently it has also been demonstrated in solution.[25] Numerous Ti precursors have been implemented to grow TiO_2 layers but titanium chloride, titanium tetraisopropoxide (TTIP) and tetrakis (dimethylamido)titanium (TDMAT) are the most commonly used (see Ref. 26 for a detailed review). In a previous study,[27] the impact of the composition of two Ti precursors (TTIP and TDMAT), the deposition temperature (T_{ALD}) and the annealing on the dielectric properties of the films have been compared. It turns out that the layers grown with TDMAT at high temperature ($T_{ALD} = 150$ °C) and annealed in air exhibit the best insulating features. In the literature, a strong influence is also observed on the photoelectrochemical properties. Various ALD processes used to grow a protective TiO_2 layer on a Si photoelectrode are listed in Table 1 of the supporting information. They lead to different layer thicknesses (t_{TiO_2}) and different photocurrents (j_{ph}). Although the conditions are not fully comparable in the Table, the wide range of j_{ph} indicates that a correlation between the synthesis parameters and the electrochemical properties could be established.

The present work is dedicated to the investigation of the electrochemical properties of n-Si/TiO_2 photoanodes. A specific experimental sequence, including cyclic voltammograms (CVs) and open circuit potential (U_{ocp}) measurements under polychromatic and monochromatic illuminations or in the dark, has been developed for this purpose as well as to assess the stability of the films. The morphology and the crystalline structure of the films are analyzed by transmission electron microscopy (TEM) and electron backscattered diffraction (EBSD). Depending on the growth parameters, an unexpected enhancement of the anodic j_{ph} is observed during the CVs for TiO_2 films synthetized with TTIP at low T_{ALD}. The (photo-)electrochemical characterizations are thus emphasized for such deposition conditions and a comparison with uncoated Si is performed to give additional insights. The influence of the thickness layer as well as the illumination wavelength on this effect is presented. Ex situ IR spectroscopy indicates that this phenomenon is related to charge accumulations within the TiO_2 layer that depends on the grain morphology. Since it is known that defects create additional energy states in the bandgap leading to an altered electrochemical response of the electrodes,[28,29] the energy band diagram, established from operando XPS measurements,[30] is used to

[a]Present address: 25 rue Eugène Combes, 19800 Corrèze, France.
[z]E-mail: lionel.santinacci@univ-amu.fr

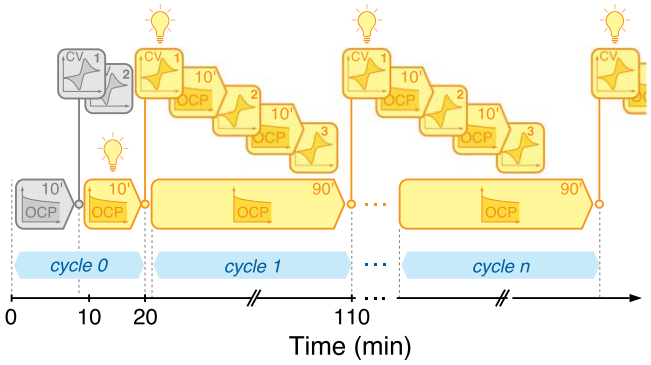

Figure 1. Timeline of the electrochemical sequence (CV and U_{ocp} measurements) applied to the samples in the dark (gray) or under illumination (yellow). The cycle 0 and the cycles 1, 2, and 3 are referred in the text.

describe the charge transfer mechanisms at the n-Si/TiO_2/electrolyte. The relations between the ALD conditions and the electrochemical properties are then presented.

Experimental

Surface preparation and ALD of TiO_2.—Experiments were carried out on n-type Si (100) (phosphorus doped, 4–6 $\Omega \cdot$ cm, from Siltronix). The wafers were cut in 1.5×1.5 cm^2 squares and degreased by sonicating in acetone, ethanol, and ultrapure water. The native oxide layer was etched by dipping the samples in 12.5% HF for 30 s. The samples were then vigorously rinsed with distilled water, dried under nitrogen and stored in a glove box. The TiO_2 thin films were grown by ALD in a Fiji 200 reactor from Veeco/Cambridge Nanotech. HCl is a by-product when using $TiCl_4$, we have therefore focused our study on TTIP and TDMAT to avoid any corrosion of the deposition chamber and pumping system. The ALD was performed using TTIP (98%, Strem Chemicals), TDMAT (99%, Strem Chemicals) and deionized water ($\rho = 18.2$ M$\Omega \cdot$ cm) according to a recipe described previously.[27] The TTIP and TDMAT canisters were heated at 85 °C. The temperature of the reaction chamber was set from 90 to 200 °C. The ALD cycle consisted of sequential pulse, exposure and purge of both Ti precursors and H_2O, alternatively. The pulse, exposure and purge durations were 2:7:15 s for the Ti precursors and 0.2:7:15 s for water. The number of ALD cycles was varied according to the growth per cycle (GPC) in order to adjust the TiO_2 thickness. The samples were annealed after the deposition at $T_a = 450$ °C in air for 2 h to transform the amorphous layer into polycrystalline anatase.

(Photo-)electrochemical measurements.—Electrochemical and photoelectrochemical investigations were carried out in a three-electrode configuration. The n-Si/TiO_2 sample was used as working electrode (back contact was established by smearing InGa eutectic). A Pt wire and a mercury/mercuric oxide electrode (Hg/HgO, 1 M KOH, $E^\circ = 140$ mV vs SHE) respectively served as counter and reference electrodes. The samples were pressed against the o-ring of the electrochemical cell leaving 0.28 cm^2 exposed to the deoxygenated electrolyte (N_2 bubbling), which consisted of 1 M KOH (analytical grade). The electrochemical cell was connected to a PAR 273 potentiostat and the setup was placed in a dark room to avoid any uncontrolled photoelectrochemical effects. During the photoelectrochemical investigations, the white light of a 150 W Xe lamp (Oriel, APEX 6255) was shined into the cell through a transparent quartz window. The light intensity was adjusted from 3 to 100 mW $\cdot$ cm^{-2} using optical filters and the calibration was carried out with a reference cell and meter (Newport, 91 150V). Monochromatic illumination was performed by placing a monochromator (Oriel, Cornerstone 130) in the optical path between the light source and the cell.

An experimental sequence has been developed to assess both chemical and (photo-)electrochemical stability of the photoanode. Figure 1 describes schematically the experimental timeline of the sequence. After the immersion in the electrolyte, the U_{ocp} of the sample is monitored in the dark for 10 min in order to reach a stable value. Then two successive voltammograms are performed in the dark and U_{ocp} is measured during 10 min under illumination to determine the photovoltage. Finally, the cycle 0 is terminated by three successive CVs under illumination. After this initial phase (cycle 0), the electrochemical sequence consists of repeatedly leaving the electrode under open circuit potential for 90 min (called illumination time, t_{light}, in the following) and performing three successive CVs under illumination separated by a 10 min U_{ocp} measurement. This cycle is reproduced n times to assess the stability of the electrode. In order to extend the experimental duration, the incident light intensity was low ($P = 3$ mW $\cdot$ cm^{-2}) to limit the potential corrosion reactions.

Structural, morphological and chemical characterizations.—The thickness of the TiO_2 thin layers has been measured by spectroscopic ellipsometry using a M-2000 V ellipsometer (J.A Woollam Co). The curve fitting was performed using the CompleteEase software applying a Cauchy oscillator model. The morphology and the crystalline structure have been analyzed by TEM using a JEM 3010 microscope (JEOL Ltd.). The cross Sections were carried out on samples prepared by ion milling with a precision ion polishing system (PIPS, M691 from Gatan Inc..). The crystallite orientation and size of the anatase films have been determined by EBSD using an e^- $Flash^{FS}$ detector (Bruker) mounted on a scanning electron microscope (JSM-7200F, JEOL Ltd.). The IR absorbance has been measured after increasing t_{light} during the photoelectrochemical sequence using a MIRacle (PIKE Technologies) attenuated total reflectance (ATR) accessory mounted in a Vertex 70 spectrometer (Bruker) equipped with a DLaTGS detector (resolution of 4 cm^{-1}).

Results

Morphology and structure of TiO_2 films.—As indicated in the introduction, the Ti precursor, the T_{ALD} and the annealing play a significant role on the electrochemical response of the TiO_2 layers grown onto n-Si. In the present work, the samples have always been annealed because as-grown layers are amorphous and they contain a variable amount of precursor ligands that are dissolved when the films are immersed in the electrolyte.[27] A contact is then established between the alkaline solution and Si through the tiny porosity of TiO_2. Si and KOH can react according to Eq. 1[31,32] and the protective layer swells and cracks quickly because H_2 accumulates at the Si/TiO_2 interface:

$$Si + 4H_2O \overset{OH^-}{\rightarrow} Si(OH)_4 + 2H_2\uparrow \quad [1]$$

Figures 2a and 2b compares the TEM cross Sections of TiO_2 films synthetized with TTIP and TDMAT after annealing. The two micrographs show similar features. The single-crystalline Si is homogeneously covered by a compact polycrystalline anatase layer. An ultrathin SiO_2 film is also visible at the n-Si/TiO_2 interface. It corresponds to the native oxide formed prior to starting the TiO_2 deposition in the ALD reactor. As expected, this thin layer (around 2 nm) is amorphous. Spectroscopic ellipso-porosimetry confirmed that the layer grown with TDMAT is not porous and it indicated a very small closed porosity in the case of TTIP.[27] In both cases, the surface is stable when it is immersed in 1 M KOH under open circuit conditions. Therefore, the thermal treatment allows for further reproducible electrochemical characterizations of n-Si/TiO_2 photoelectrodes.

The crystallite orientation and size have been analyzed by EBSD. Figures 2c and 2d show the grain views for anatase films deposited on Si(100) using TTIP and TDMAT. No significant variations in the orientation are found when comparing the two layers. This is

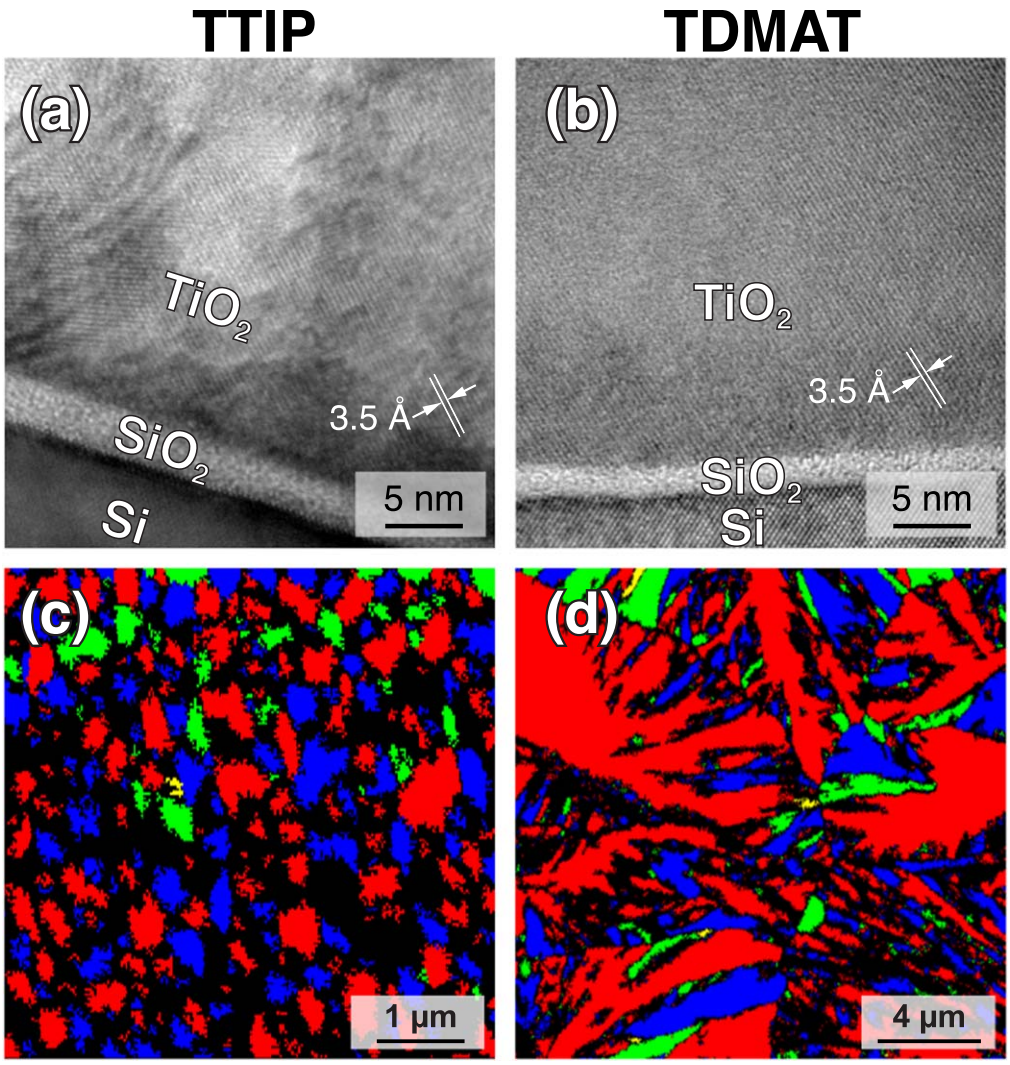

Figure 2. Comparison of 50 nm-thick TiO_2 layers grown on Si(100) at T_{ALD}=120 °C using the two Ti precursors after annealing in air at $T_a = 450$ °C for 2 h. TEM cross Sections for TTIP (a) and TDMAT (b). The interplanar distances are indicated on each TEM image. They are similar and correspond to (101) planes. EBSD grain top views for TTIP (c) and TDMAT (d).

detailed on the inverse pole figures shown on Fig. S1 (available at stacks.iop.org/JES/168/031509/mmedia) in supplementary information. However, the crystallite average size is approximately 0.35 μm for TTIP and larger than 3.5 μm for TDMAT at $T_{ALD} = 120$ °C. The film grown using TTIP contains therefore more grains boundaries (approximately 10 more according to the simple calculation proposed in Fig. S2) than its equivalent synthesized with TDMAT.

Electrochemical investigations.—Figure 3 shows voltammograms of TiO_2 thin films grown on n-Si using TTIP and TDMAT at different T_{ALD}. Depending on the precursor type and the deposition temperature two different photocurrent evolutions are observed. When using all Ti precursors at high T_{ALD} (i.e. TDMAT at $T_{ALD} = 120$ and 150 °C or TTIP at $T_{ALD} = 200$ °C), the onset potentials for oxidation (U_{ox}) are located between −1 and −0.75 V and the voltammograms exhibit a photocurrent plateau in the range of 60 to 140 $\mu A \cdot cm^{-2}$. In the case of low temperature using TTIP (i.e. TTIP grown at $T_{ALD} = 120$ °C), the onset is much more anodic ($U_{ox} \approx 0$ V) and no j_{ph} plateau is observed. This curve is very similar to a previous study in which TiO_2 was grown using $TiCl_4$ on Si nanopilars.[23] No photocurrent plateau was observed and the authors proposed a degradation mechanism based on the deterioration of the TiO_2 at $pH = 14$. These different behaviors

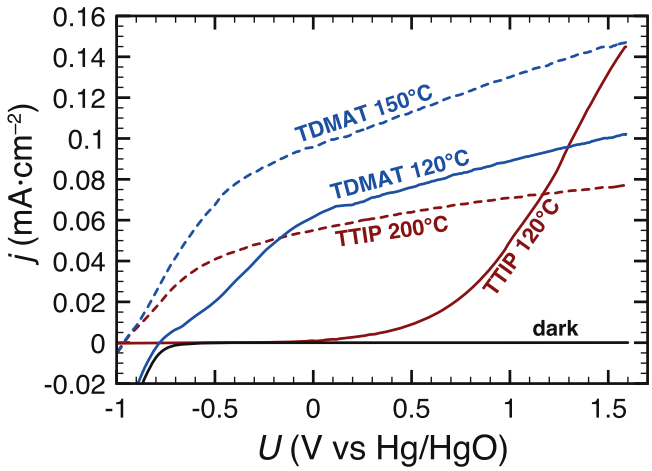

Figure 3. Linear sweep voltammetries of n-Si/TiO_2 photoanodes in 1 M KOH under illumination ($P = 100$ mW · cm^{-2}). The 35 to 40 nm-thick TiO_2 films were grown using different Ti precursors (TTIP and TDMAT) at different T_{ALD} as indicated on the plot. A voltammogram measured in dark conditions is plotted as reference. The scan rate is 20 mV · s^{-1}.

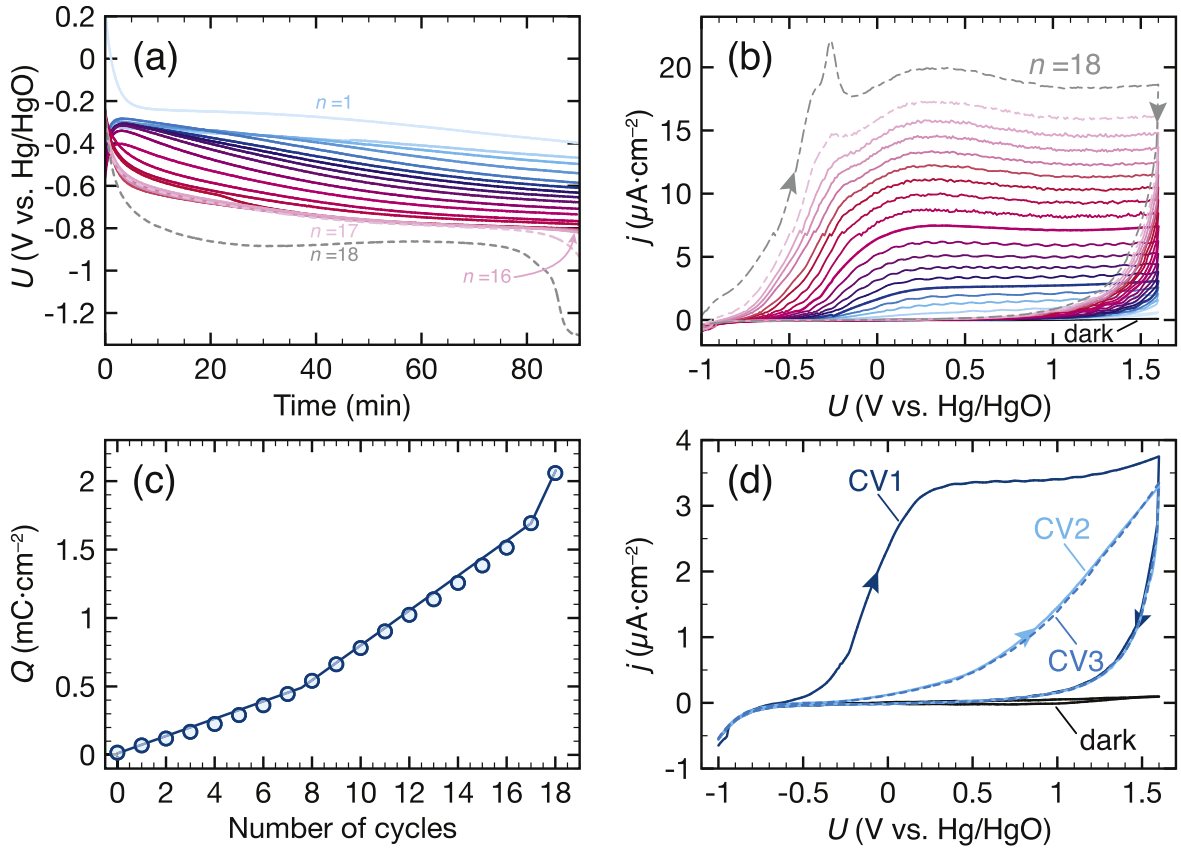

Figure 4. Electrochemical response of n-Si coated by a 40 nm-thick TiO_2 layer grown on n-Si using TTIP at $T_{ALD} = 120$ °C. (a) U_{ocp} against time under illumination ($P = 3$ mW · cm^{-2}) from $n = 1$ to 18. (b) CVs under illumination acquired after each U_{ocp} measurement. (c) Anodic charge extracted from the CV curves plotted against n. (d) Three successive CVs for $n = 5$. The CV measured in the dark is added for comparison.

could arise from variations in the film composition, morphology or crystalline structure. As mentioned above, it has been demonstrated that the dielectric properties of such films are indeed strongly influenced by the Ti precursor composition and the deposition temperature.[27] This was ascribed to the incorporation of the isopropoxyl ligands in the layer when using TTIP while almost no amines were trapped using TDMAT. In the case of TTIP, ALD at higher temperatures ($T_{ALD} > 200$ °C) led to a lower amount of trapped ligands and the post-deposition annealing allowed for removing significantly the incorporated molecules. The electric properties of such layers were drastically improved but the TDMAT-based films still exhibited better performances. Those conclusions are well in line with the photoelectrochemical properties of the TiO_2 layers shown in Fig. 3, which will be explained in the following.

In order to identify the origin of the differences revealed in Fig. 3, we have drawn a specific attention to the photoelectrochemical properties of TTIP-based layers since they show an unusual behavior. The experimental sequence, described in Fig. 1, has been applied, with a low illumination power, to a n-Si wafer covered by a 40 nm-thick TiO_2 layer grown using TTIP at $T_{ALD} = 120$ °C. U_{ocp} is plotted against time for each step of the electrochemical sequence on Fig. 4a while the corresponding CVs are presented on Fig. 4b. U_{ocp} measured in the dark and under illumination during the initial cycle ($n = 0$) is shown in Fig. S3. As expected for a n-type semiconductor the U_{ocp} is negatively shifted under illumination. The photovoltage ($\Delta U_{ocp} = U_{ocp}^{dark} - U_{ocp}^{light}$) is around − 0.3V. However, the electrochemical response presented in Fig. 4 is not expected since U_{ocp} decreases progressively after each step (Fig. 4a). It starts around −0.2 V for $n = 1$ and moves to −0.7 V for $n = 16$. This phenomenon is coupled with a spectacular improvement of the j_{ph} plateau on Fig. 4b (from $j_{ph} = 0.5$ to 20 μA · cm^{-2}) and a progressive cathodic shift of the onset potential (Fig. S4 shows normalized CVs) that leads to a better fill factor. Surprisingly, the CVs show a strong hysteresis. The photocurrent decreases rapidly on the reverse scan and reaches the level of the dark current.

The j_{ph} enhancement has been quantified by calculating the anodic charge (Q) passed during the CV.[33] Q is plotted against n on Fig. 4c. It progressively rises exhibiting an inflexion around $n = 8$ with no obvious correlation with any specific evolutions of the curves presented in Figs. 4a and 4b. A second evolution within the curve occurs for $n = 18$ where Q increases significantly. It is related, here, to the anodic peak that arises on the CVs around −0.3 V for $n \geqslant 17$. Successives CVs have also been performed during the same cycle (constant n). Figure 4d shows a sequence of three successive CVs measured at $n = 5$ (noted CV1, CV2 and CV3 on the plot). CV1 corresponds to the voltammogram shown on Fig. 4b for $n = 5$. After a cathodic current measured between $U = -1$ and −0.7 V that can be ascribed to the reduction of water, the photocurrent, corresponding to an oxidation process (that will be defined later), is initiated around $U_{ox} = -0.5$ V and a photocurrent plateau is observed at $j_{ph} = 3.5$ μA · cm^{-2} between $U = 0.25$ and 1.6 V. As observed on Fig. 4b, the current drops rapidly on the reverse scan. CV2 and CV3 are similar but exhibit a different evolution as compared to CV1. Although no variation is visible on the cathodic current, the onset potential for the oxidation process is shifted to more positive potentials and no plateau is detected. Again, the current diminishes quickly and reaches the level of the dark current on the reverse scan.

Additional evolutions are observed on Figs. 4a and 4b when $n > 16$. A steep decrease of U_{ocp} occurs after 70 min for $n = 17$ and 18 and it stabilizes around −1.3 V (Fig. 4a). Simultaneously, the CVs for $n = 17$ and 18 exhibit the previously mentioned anodic peak centered at −0.3 V (Fig. 4b). At that time of the electrochemical

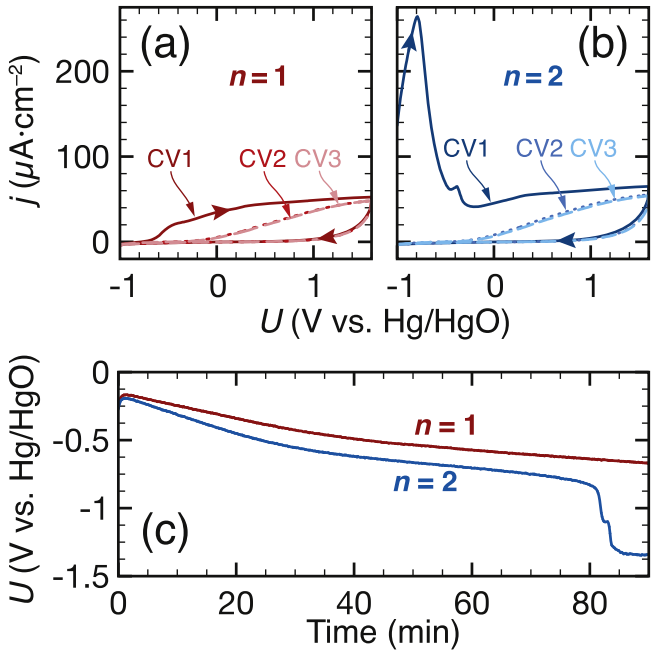

Figure 5. CVs under illumination for n-Si/SiO_2 in 1 M KOH for $n = 1$ (a) and $n = 2$ (b). Open circuit potential against time under illumination for $n = 1$ to 2 ($P = 3$ mW · cm^{-2}).

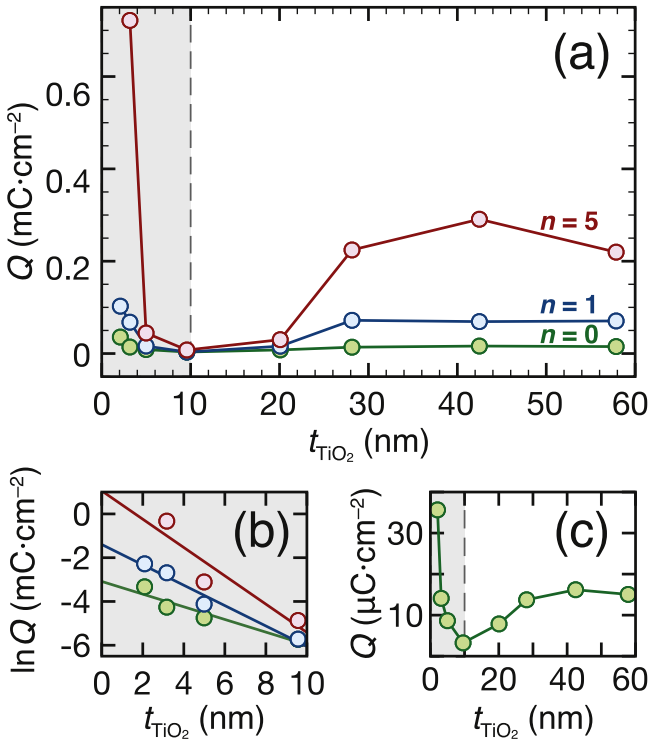

Figure 6. (a) Evolution of the anodic charge with the TiO_2 thickness for $n = 0$, 1 and 5. (b) ln Q vs t_{TiO_2} (from 0 to 10 nm) corresponding to the decay region highlighted in gray on (a). (c) Enlarged view of the curve for $n = 0$ shown in (a). TiO_2 has been grown using TTIP at $T_{ALD} = 120$ °C.

sequence (i.e. after U_{ocp} reaches −1.3 V), the surface was strongly degraded and an intense bubbling was observed at the working electrode. The current became highly erratic and finally, it was necessary to stop the experiment after $n = 19$ (for the sake of clarity, the CV for $n = 19$ is shown in Fig. S5). When the sample was removed from the cell, a strong degradation of the exposed area was noticed. The TiO_2 layer was partially lifted off (Fig. S6).

Similar experiments have been carried out on n-Si. In order to properly compare with the results presented in Fig. 4, the native oxide layer has not been removed by HF dip prior to the experiments. A thin SiO_2 layer is, indeed, formed between n-Si and TiO_2 during the ALD process (see Fig. 2) and it should be present on n-Si for a rigorous comparison. Figure 5 shows CVs and U_{ocp} monitoring for $n = 1$ and 2 on n-Si/SiO_2. For $n = 1$, the surface exhibits, surprisingly, a similar behavior as n-Si/SiO_2/TiO_2. On the first CV (Fig. 5a) the photocurrent reaches a plateau ($j_{ph} \approx 50\ \mu A \cdot cm^{-2}$) and drops to zero on the reverse scan. The successive CVs do not show this plateau. U_{ocp} starts at −0.2 V and decreases progressively with time to reach −0.7 V (Fig. 5c). For $n = 2$, the first voltammogram (CV1 on Fig. 5b) displays a strong anodic peak centered at −0.8 V. Similarly to the case $n = 1$, j_{ph} becomes almost constant for further anodic polarizations and the following voltammograms (CV2, CV3) do not exhibit any current plateau. Although U_{ocp} starts from the same value (Fig. 5c), it decreases somewhat more quickly for $n = 2$ and drops steeply after 80 min to finally stabilizes around −1.35 V after 85 min.

These experiments have been repeated, for comparison, on H-terminated Si immersed in KOH. The results shown on Fig. S7 are very similar to Fig. 5b and to the literature. When a positive bias is applied to H-terminated n-Si, an anodic peak around − 0.85V is indeed observed and U_{ocp} is constant at −1.25 V.[34] Several exhaustive investigations of the oxidation of Si in KOH and NaOH have been performed previously.[31,32,34–41] They have led to clear descriptions of the etching and passivation processes that take place on Si in such alkaline solutions. To put in a nutshell, under anodic polarizations, Si is first etched up to the anodic peak, then the surface is passivated and the following constant current corresponds to the growth of the SiO_2. The current is much lower on the reverse scans as well as on the following voltammogram because Si is already covered by its oxide. When Si is cathodically polarized, the SiO_2 layer is etched. This simplified picture explains the absence of the anodic peak for $n = 1$ (Fig. 5a) while it is present for $n = 2$ (Fig. 5b). As mentioned before, Si is covered by its native oxide layer (Fig. 5a) and therefore no passivation peak can be observed. When the sample is left under illumination at open circuit conditions, the potential is more negative and the oxide is dissolved. A passivation peak is naturally observed for $n = 2$ (Fig. 5b). Note that the dissolution of the SiO_2 is not uniform. It rather proceeds by random pitting.[40]

The observations carried out on n-Si (with and without native SiO_2) give valuable information to explain some electrochemical evolutions of the n-Si/TiO_2 system shown in Fig. 4. The anodic peak appearing at −0.3 V for $n \geqslant 17$ is ascribed to the passivation of the Si. The CV for $n = 19$ (Fig. S5) exhibits a wider anodic wave centered at a potential that fits properly with the passivation peak of Si. The presence of the peak on the CVs occurs when U_{ocp} reaches 1.25 V. This value indicates that Si in contact with the electrolyte and that TiO_2 is, at least, partially removed or porous at that time.

The effect of the thickness of the TiO_2 layer on the anodic photocurrent has been investigated. Figure 6 shows the anodic charge against t_{TiO_2} for $n = 0$, 1, and 5 (similar evolutions are observed for other values of n but they are not shown for the sake of clarity). As expected from the voltammograms presented in Fig. 4b, Q increases with n. This tendency is also observed on Fig. 6 but the three curves exhibit a similar trend: from 0 to 10 nm, Q drops quickly to zero, then it progressively increases and reaches a plateau from 30 to 60 nm. Since the values for $n = 0$ are not easily visible on Fig. 6a, an enlarged view is plotted on Fig. 6c and the similar evolution is confirmed. The ln Q vs t_{TiO_2} is plotted on Fig. 6b for the thinnest films (the gray area on Figs. 6a and 6c). The linear evolution demonstrates that Q exponentially decays for $t_{TiO_2} < 10$ nm. It suggests that the anodic photocurrent proceeds according to a tunneling mechanism from the n-Si to the electrolyte through the TiO_2 layer. When the layer gets thicker ($t_{TiO_2} \geqslant 10$ nm), the carriers cannot be transferred anymore and no current is measured.[42] For thicker films ($t_{TiO_2} > 20$ nm), the charges that reach the electrolyte

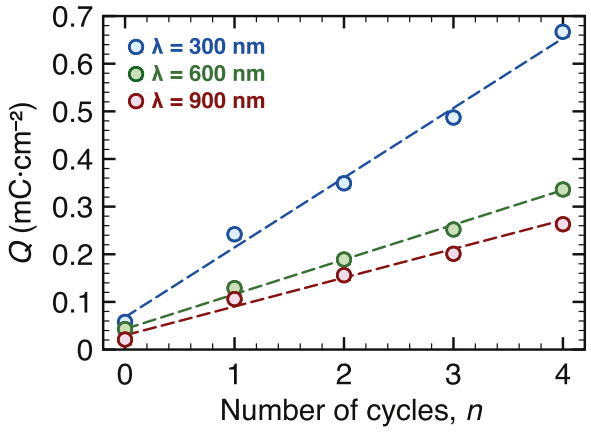

Figure 7. Comparison of the evolution of the anodic charge against n for various λ. The 40 nm-thick TiO_2 layer is grown using TTIP at $T_{ALD} = 120$ °C.

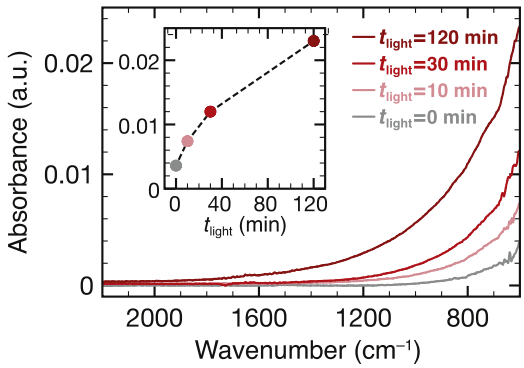

Figure 8. ATR-IR spectra of TiO_2 thin films on Si after increasing illumination time (indicated on the plot). The inset shows the absorbance evolution with t_{light} at 600 cm^{-1}. The 40 nm-thick film was grown using TTIP at $T_{ALD} = 120$ °C.

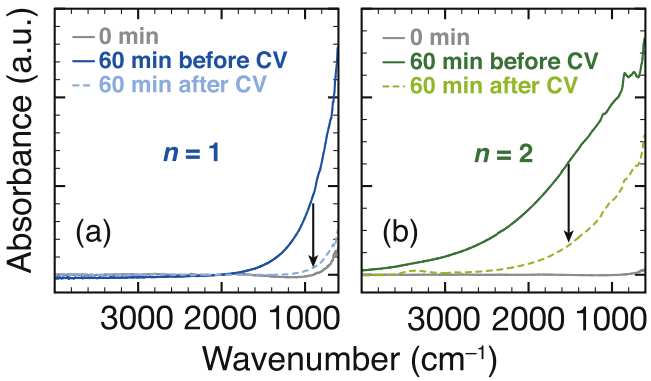

Figure 9. Comparison of the ATR-IR spectra of TiO_2 thin films on Si for $t_{light} = 60$ min before and after the CV for $n = 1$ (a) and $n = 2$ (b). The reference absorbance ($t_{light} = 0$ min) is shown in gray on both plots. The 40 nm-thick film was grown using TTIP at $T_{ALD} = 120$ °C.

come either from the Si or from the TiO_2 but there is no current tunneling because the film is too thick. Another charge transfer mechanism will be proposed in the discussion section.

The electrochemical sequence presented in Fig. 1 has been slightly modified in order to determine the origin of the photocarriers leading to the photocurrent. The samples were illuminated with a monochromatic light at different wavelengths. Figure 7 shows the evolution of Q against n for $\lambda = 300$, 600 and 900 nm. As expected from Fig. 4c, a linear increase is observed for all wavelengths but the starting values and the slopes decrease with λ. As mentioned before, the anodic charge reflects the variation of the photocurrent. The highest j_{ph} is measured when the sample is illuminated in the UV range. At this wavelength, the e^-/h^+ pairs can be photogenerated in both TiO_2 and Si because the energy ($E = 4.14$ eV) is higher than the E_g of both semiconductors. Conversely for the longer λ, the carriers are solely generated in Si. When considering the penetration depth of the light (α^{-1}) for λ=300 nm, it appears that photons are absorbed only (or at least mainly) within TiO_2 since $\alpha^{-1} < 40$ nm (see e.g. [43]). This indicates that j_{ph}, measured under white light, originates from the sum of the photoexcitations occurring in both Si and TiO_2. Depending on the wavelength, the e^-/h^+ pairs are generated in Si or TiO_2 but more carriers are produced or collected when the photons are absorbed in TiO_2. This could be explained by the necessity for the charges produced in Si to cross the oxide prior to be injected in the electrolyte (tunneling is neglected for such thick TiO_2 layers).

IR spectroscopy.—The enhancement of the photocurrent at TiO_2 electrodes has been reported previously.[44–47] It was ascribed to hydrogen insertion within TiO_2 after a cathodic polarization or illumination at U_{ocp} called electrodoping or photodoping, respectively.[46] The H-doping under cathodic bias has been described earlier by Dyer and Leach using Eq. 2:[48,49]

$$Ti^{IV}O_2 + e^- + H^+ \rightarrow Ti^{III}(O)(OH) \quad [2]$$

This phenomenon has been explained by coupling electrochemical characterizations with in situ and ex situ IR spectroscopic measurements[46,50,51] as well as DFT calculations.[47] It is affected by the cathodic polarization (duration and potential),[44,51] the light exposure duration[52] and the TiO_2 morphology (e.g. nanoparticules, nanotubes, compact film).[46,47] Similar ex situ ATR-IR analyses are shown in Fig. 8 for $t_{light} = 0$, 10, 30, 120 min. The structureless absorbance increases continuously toward lower wavenumbers with t_{light}. It is further visible on the inset that shows the signal evolution at 600 cm^{-1}. This broad increase has been ascribed to the accumulation of electrons below E_F in the TiO_2 films leading to localized Ti^{3+} sites and the concomitant insertion of charge-compensating protons.[46,53] The e^-/H^+ are mainly concentrated at particle/particle interfaces, pores or grain boundaries (GB). According to our previous study,[27] depending on the ALD paramaters, the films can contain pores and a variable density of GBs.

As mentioned above, such doping arises from a reductive potential and/or illumination at U_{ocp}. It is persistent until an anodic polarization is applied to the sample. Figure 9 presents the IR absorbance for n-Si/TiO_2 after $t_{light} = 60$ min before and after a CV. For $n = 1$ (Fig. 9a), the absorbance increases after the photodoping step and drops almost back to the initial signal after the anodic sweep. For $n = 2$ (Fig. 9b), the signal is further increased and the remaining absorbance is higher than the previous cycle. It indicates that an anodic sweep can partially remove the accumulated charges. However, the doping cannot be fully suppressed within the time scale of some CVs because the slow kinetics of the H^+ diffusion from the film to the electrolyte is the limiting step.[47] Consequently, the persistent hydrogen uptake grows continuously with n during the electrochemical sequence. The enhancement of j_{ph} has been ascribed to the filling of the pores or GBs by e^-/H^+ during the illumination step leading to the deactivation of the traps.[46] Therefore, the higher j_{ph} could arise from a faster electron transfer through those locations and less e^-/h^+ recombinations.[47] This is supported by other works that have evidenced similar findings after H- or Li-doping of TiO_2.[45,54,55] The electrochemical doping process is slow because it is limited by the diffusion of the hydrogen within the TiO_2 layer. Similarly, the dedoping is controlled by the kinetics of H^+ diffusion in the grain boundaries to the solution.[47] Since the anodic polarization applied during the CV is short, a persistent hydrogen uptake occurs for each cycle of the electrochemical sequence. This induces a progressive increase of the remaining doping in the electrode and

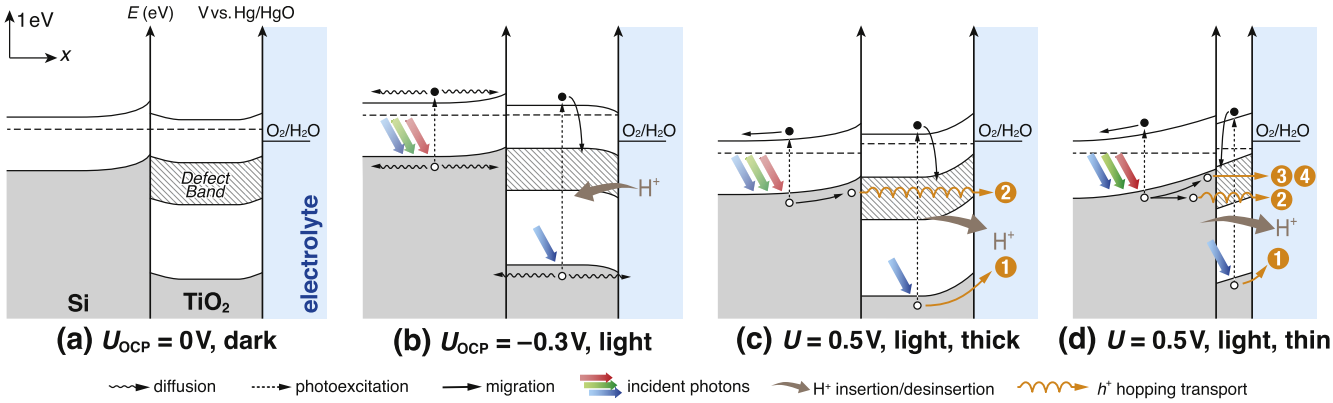

Figure 10. Energy band diagrams of the n-Si/TiO_2/electrolyte junction for various conditions. The band positions have been determined from Ref. 30. The defect band (hatched area) is drawn in the bandgap of TiO_2 according to the literature.[30,59,60] Junction in the dark at U_{ocp} (a). Junction under illumination at U_{ocp} (b), at $U = 0.5$ V for thick (c) and thin (d) layers. The e^- and h^+ are drawn as filled and open circles, respectively. The hole transfer mechanisms from the electrode to the solution under anodic polarization are shown on the diagrams: hole injection ①, hopping transport ②, tunneling ③ and defect-mediated transfer ④.

leads therefore to the continuous enhancement of j_{ph} as observed on Figs. 4b and 4c.

Discussion

Interpretation of the anodic currents.—Some of the results reported in the previous Section require further interpretations: (*i*) the more positive U_{ox} for TiO_2 layers grown using TTIP at 120 °C (Fig. 3), (*ii*) the enhancement of j_{ph} with n (Fig. 4b) and (*iii*) the different evolutions of j_{ph} with t_{TiO_2} (Fig. 6). The energy band diagrams established from in operando XPS[30] shown in Fig. 10 are used to elucidate the charge transfers at the n-Si/TiO_2/electrolyte junction for specific potentials in the dark or under illumination.

- At U_{ocp}, in the dark (Fig. 10a), there is no electron in the conduction band (CB) of both n-Si and TiO_2. Due to the position of U_{ocp} with respect to the CB edge of TiO_2, there is no chance for an electron to be injected from the electrolyte to TiO_2. In this situation, no effective current is measured and H-doping does not take place.
- At U_{ocp}, under illumination (Fig. 10b), the photovoltage shifts the bands upward and e^-/h^+ pairs are created in n-Si and TiO_2. Since the bands are almost flat, the photocarriers diffuse in both semiconductors. The electrons located in the CB of TiO_2 can relax in the defect band located below[56] and the holes can be injected in the electrolyte. This excess of negative charges in the film is compensated by H^+ insertion within TiO_2 according to Eq. 2.[46] The electrons photogenerated in n-Si can either recombine or diffuse into the CB of TiO_2 and further increase the accumulation. Again no external current is measured but H-doping proceeds. Note that, for sufficiently thin TiO_2 layers, the H can also reach n-Si[39] constituting therefore a supplementary doping reservoir.
- When considering the system under polarization and illumination, a photocurrent is measured. One has to take into account the thickness of the film because Q varies with t_{TiO_2} differently for thin and thick layers (i.e. $t_{TiO_2} > 10$ nm and $t_{TiO_2} < 10$ nm, respectively). Figure 10c presents the band diagram for a thick TiO_2 film. Photocarriers are created in TiO_2 as well as in n-Si. The photoholes generated in the valence band (VB) of TiO_2 under UV light ($\lambda < 390$ nm) are directly injected into the solution: mechanism ①. They contribute to water oxidation (Eq. 3):

$$4OH^- + 4h^+ \rightarrow O_2 \uparrow + 2H_2O \qquad [3]$$

The photoholes created in the n-Si undergo the electric field of the space charge layer (SCL) and are injected in the defect band of the TiO_2 where they can either recombine with photoelectrons of the CB

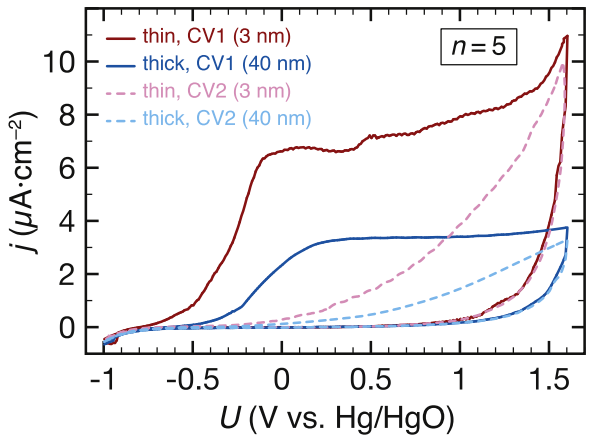

Figure 11. CVs under illumination ($P = 3$ mW · cm^{-2}) of n-Si coated by thin ($t_{TiO_2} = 3$ nm) and thick ($t_{TiO_2} = 40$ nm) TiO_2 layers grown using TTIP at $T_{ALD} = 120$ °C ($n = 5$).

or react with $Ti^{III}(O)(OH)$: mechanism ②. This leads to the dedoping process according to Eq. 4 instead of water oxidation.

$$Ti^{III}(O)(OH) + h^+ \rightarrow Ti^{IV}O_2 + H^+ \qquad [4]$$

- The band diagram for thin TiO_2 layers is presented in Fig. 10d. In this case, the photocarriers are mainly generated in the n-Si. The small amount of holes created in TiO_2 is still injected in the solution to oxidize water via mechanism ① but it contributes slightly to the whole current. As mentioned earlier, the H-insertion can proceed in the Si. This phenomenon is, of course, enhanced for thin TiO_2 layers. The h^+ photogenerated in the n-Si react therefore with the hydrogen atoms according to Eq. 5:

$$Si(H) + h^+ \rightarrow Si + H^+ \qquad [5]$$

The H^+ migrate from the n-Si to the solution, through TiO_2, under the electric fields of the SCLs of both semiconductors. The dedoping process originates mainly from n-Si in this situation. In addition to mechanisms ① and ②, the measured current comes also from the direct injection of h^+ from n-Si to the electrolyte according to two pathways.[57] The photoholes are transferred to the solution either by direct tunneling (mechanism ③) across TiO_2[58] or by defect-mediated transport (mechanism ④) through the defect band. The decoration of the GB with e^-/H^+ inserted during the illumination at U_{ocp} further enhances mechanism ④ since they deactivate numerous interface traps and recombination sites.[47] These two mechanisms lead to water

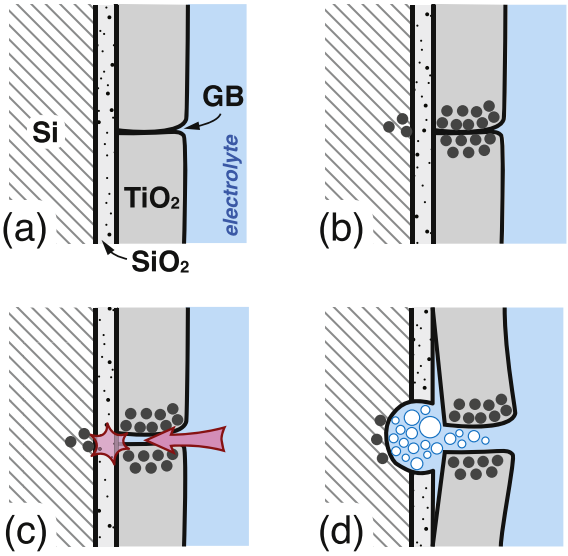

Figure 12. Scheme of the degradation mechanism of n-Si/TiO_2. (a) Initial view of a GB in contact with the electrolyte. (b) Accumulation of e^- and charge-compensating H^+ (●) at the GB. (c) After several electrochemical cycles leading to the GB embrittlement, contact between Si and electrolyte is established. (d) Etching of the n-Si substrate and H_2 bubbling (white circles) at the n-Si surface inducing the swelling of the TiO_2 layer.

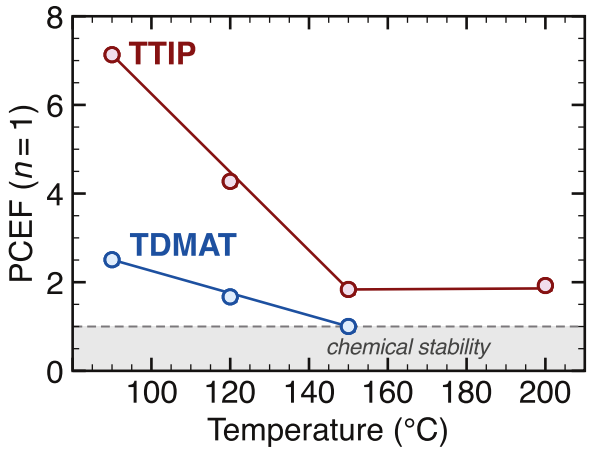

Figure 13. PCEF (n = 1) against T_{ALD} for TiO_2 grown using TTIP and TDMAT. When PCEF ⩽ 1, it means that no photocurrent enhancement is measured. The PCEF has been calculated for $n = 1$. The film is stable (the gray area on the plot). The number of ALD cycles has been adjusted to grow 40 nm-thick layers because the GPC depends on the Ti precursor composition and T_{ALD}.

oxidation and, as indicated in Fig. 6, they enhance j_{ph} in comparison to thick layers. This is also clearly illustrated on Fig. 11 which compares the CVs for n-Si coated by a thin and a thick TiO_2 layer ($t_{TiO_2} = 3$ and 40 nm, respectively) at $n = 5$ cycles. The j_{ph} plateau is approximately twice as high for the thin layer as for the thick one (the other evolutions of the CVs remain nevertheless similar). In both cases, the plateau corresponds mainly to the dedoping process while water oxidation contributes slightly to the measured j_{ph} at larger overvoltages. Mechanism ② is in line with the hysteresis observed on the first CVs. During the forward scan, a large amount of H is extracted from TiO_2 and/or n-Si to the solution. On the reverse scan and the following CVs, the current is very low because it becomes difficult to take out the remaining H since their transport is limited by diffusion. For thin TiO_2 layers, the Si(H) reservoir can no longer supply protons, because the SCL has been emptied during the forward scan. Consequently, the U_{ox} is shifted to a more positive potential on CV2 where j_{ph} corresponds to the water oxidation. The hysteresis, observed on the first CVs, demonstrates the critical role of the SCLs in TiO_2 and n-Si to extract the H inserted during the doping step. Except the tunneling processes (③ and ④), the charge transfers are similar in thin and thick layers. However, the H-doping takes place mainly in TiO_2 in thick layers while it is mostly located in n-Si for thin films. In both situations, the H-desinsertion is caused by the illumination and the electric field in both SCLs.

The dedoping process ④ is observed in the present study because the CVs have been performed at a low illumination power ($P = 3\ mW \cdot cm^{-2}$). At higher illumination flux, it is hidden by the water oxidation. It explains why this phenomenon has not been reported in previous works carried out at a much stronger irradiance ($P = 500\ mW \cdot cm^{-2}$).[44,50] Note also that the capacitive current usually measured on the cathodic part of the CVs[44] has not been observed during this work. This is mainly due to the morphology of the present films that exhibit a much smaller active area as compared to the nanostructured TiO_2 used by Berger et al.[44] In addition, the present observations could explain the instability reported, by Pavlenko et al.,[23] for TiO_2 films grown using $TiCl_4$ as well as similar doping processes depicted on other metal oxides such as WO_3.[61]

Film degradation mechanism.—Depending on the growth parameters and thickness, the films degrade after a variable number of cycles (e.g. $n = 19$ for a 40 nm-thick film grown using TTIP at 120 °C). The H-doping occurs indeed mainly at particle/particle interfaces, pores and GBs. The present layers are compact (i.e. they do not consist of particles) but, depending on the growth conditions, they include a variable concentration of pores and GBs. As shown in a previous work,[27] open porosity can be observed for as-grown samples but the pores are closed during the annealing. Such thermal treatment has been carried out for all films to avoid any direct deleterious contact between the silicon and the electrolyte. Figure 12 describes schematically the degradation process. The H-doping of the TiO_2 films is therefore localized in the closed pores and at GBs (Fig. 12b). The hydrogen accumulation as well as its diffusion in and out of the film generate mechanical stress (hydrogen embrittlement[42]) leading to the formation of tiny breaks and pores (Fig. 12c). A silicon/electrolyte contact is therefore established (red sparkle and arrow on Fig. 12c) and the usual corrosion process proceeds (Fig. 12d). As indicated by Eq. 1, H_2 is produced and the gas bubbling at the n-Si surface causes the swelling of the TiO_2 layer. This phenomenon is initially localized but it results in the full removal of the film.

For thin layers, hydrogen incorporation also proceeds into Si. The film destruction arises therefore mainly from the H transport through the film. According to a previous study performed on Si in KOH,[39] when the hydrogen incorporation reaches a sufficient amount, it is associated with mechanical stresses that lead to the formation of microcracks and surface roughening. The first inflection point observed in Fig. 4c (for $n = 7$–8) could therefore be attributed to this surface roughening at the n-Si/TiO_2 interface. This tiny increase of the active area could indeed cause a slight j_{ph} rise. This phenomenon occurs obviously prior to reach the deterioration step described above. The best corrosion protection is thus achieved when ALD of TiO_2 is performed with TDMAT at $T_{ALD} = 150$ °C because it limits those detrimental effects.

ALD synthesis parameters and electrochemical response.—The photocurrent enhancement depends strongly on the ALD conditions. Similar to a previous work,[46] we have determined the photocurrent enhancement factor (PCEF) to quantify and compare the j_{ph} increase. In the present case, the ratio is calculated using the anodic charge (instead of j_{ph}) for the cycle n divided by the initial value Q_0 for $n = 0$:

$$PCEF(n) = \frac{Q(n)}{Q_0} \quad [6]$$

Figure 13 shows the evolution of PCEF for TiO_2 films grown either using TTIP or TDMAT for an increasing T_{ALD} ($n = 1$). In either

case, the PCEF decreases with increasing T_{ALD}. However the enhancement is significantly stronger when using TTIP. This can be easily correlated to morphology of the film that has been fully described in our previous work.[27] At low deposition temperature with TTIP, the TiO_2 film contains some tiny closed pores and, as seen on Fig. 2, the crystallite size is much smaller than with TDMAT. Since the H-doping process is mainly localized at those locations, it is greater with TTIP at low T_{ALD}. When the deposition temperature increases the pore concentration decreases while the crystallite size grows. The PCEF is thus progressively quenched. A similar trend is observed for TDMAT but since the film quality is notably higher with this precursor (no porosity and large crystallite size), the PCEF is lower and it reaches rapidly 1 (the gray area on the plot highlights the stability of the films). At this value, no photocurrent enhancement occurs and the films are stable. Note that using TTIP, the PCEF never reaches 1. It means that the j_{ph} enhancement remains, leading to not perfectly stable TiO_2 layers.

The photocurrent enhancement observed with TiO_2 films grown with TTIP at low T_{ALD} could be seen as beneficial. However, it is not because it corresponds to the dedoping process rather than to the water photo-oxidation. It is only observed at low illumination power while in conditions closed to the solar irradiance (Fig. 3), the performances are significantly lower than for the films deposited with TDMAT. The photocurrent increase is even detrimental because it is coupled with the hydrogen insertion/desinsertion that weakens the film and leads to the corrosion of n-Si. The numerous defects of TiO_2 using TTIP at low T_{ALD} induce carriers recombinations. They are the main limitation to the water photo-oxidation observed in Fig. 3. To optimize the electrode performances, it is necessary to have a compact TiO_2 film with a low GB density that limits the H-insertion and exhibits less recombination centers. ALD of TiO_2 using TDMAT at high T_{ALD} is therefore the most suitable.

Conclusions

The present work evidences the direct correlation between the synthesis conditions of the protective TiO_2 deposited on n-Si and the electrochemical properties of such composite electrode. Various responses are indeed measured depending on the Ti-precursor composition and the T_{ALD}. This is ascribed to the insertion of e^- and charge-compensating H^+ when the electrodes are left at U_{ocp} under illumination. This process occurs preferentially at the grain boundaries and pores. It is therefore enhanced in TiO_2 grown using TTIP at low T_{ALD} because these films contain a high density of such defects. Depending on t_{TiO_2}, four charge transfer mechanisms have been identified to explain the measured anodic photocurrent. In all cases, holes photogenerated in TiO_2 are injected in the electrolyte leading to water oxidation (mechanism ①). In addition to this minor contribution to j_{ph}, H-desinsertion proceeds simultaneously and participates mainly to the current flow (mechanism ②). However for thick layers, the extracted hydrogens come mostly from the TiO_2 while they originate from the n-Si for ultrathin films. When the films are sufficiently thin (i.e. less than 10 nm), water oxidation occurs also because holes are directly injected from n-Si to the solution by tunneling and defect-mediated transport (mechanisms ③ and ④, respectively). It is the H-dedoping process that causes the photocurrent enhancement observed on the forward scans of the first CVs when the films are deposited using TTIP at low T_{ALD}. In this case, the films exhibit, indeed, numerous GBs and closed pores that host the hydrogens atoms or those defects facilitate the H-transport for the insertion into n-Si.

These results are interesting because they can help with predicting the electrochemical stability of protective layers according to their microstructure. They also show that the stability of photoelectrodes should not be assessed only under operating conditions (i.e. polarization and AM 1.5 illumination) but the testings should also include U_{ocp} measurements in the dark and under low illuminations to explore all the possible processes.

Acknowledgments

The authors are indebted Dr. Gabriel Loget (CNRS – University of Rennes 1, Rennes) for fruitful discussions and to Y. Samih and P. Lasson (Synergie 4, Evry, France) for EBSD analysis. D. Ferry and D. Chaudansson (CNRS – Aix-Marseille Univ., France) are acknowledged for their meticulous help in electron microscopy and FTIR experiments. M. E. Dufond is indebted to the Ministry of Higher Education, Research and Innovation (Doctoral School ED352 of the Aix-Marseille Univ.) for his PhD grant.

ORCID

Lionel Santinacci https://orcid.org/0000-0002-7250-0704

References

1. A. Fujishima and K. Honda, *Nature*, **238**, 37 (1972).
2. B. A. Pinaud et al., *Energy Environ. Sci.*, **6**, 1983 (2013).
3. J. W. Ager, M. R. Shaner, K. A. Walczak, I. D. Sharp, and S. Ardo, *Energy Environ. Sci.*, **8**, 2811 (2015).
4. S. Ardo et al., *Energy Environ. Sci.*, **11**, 2768 (2018).
5. K. Sun, S. Shen, Y. Liang, P. E. Burrows, S. S. Mao, and D. Wang, *Chem. Rev.*, **114**, 8662 (2014).
6. G. Loget, *Current Opinion in Colloid & Interface Science*, **39**, 40 (2019).
7. L. Santinacci and T. Djenizian, *C. R. Chimie*, **11**, 964 (2008).
8. G. Ling-Ju, L. Jun-Wei, H. Tao, W. Su-Huai, and L. Shu-Shen, *Phys. Rev. Appl.*, **10**, 064059 (2018).
9. G. Hodes, L. Thompson, J. DuBow, and K. Rajeshwar, *J. Am. Chem. Soc.*, **105**, 324 (1983).
10. T. Osaka, *J. Electrochem. Soc.*, **131**, 1571 (1984).
11. R. C. Kainthla, *J. Electrochem. Soc.*, **133**, 248 (1986).
12. A. Q. Contractor and J. O. Bockris, *Electrochim. Acta*, **29**, 1427 (1984).
13. M. J. Kenney, M. Gong, Y. Li, J. Z. Wu, J. Feng, M. Lanza, and H. Dai, *Science*, **342**, 836 (2013).
14. Y. J. Hwang, A. Boukai, and P. Yang, *Nano Lett.*, **9**, 410 (2009).
15. M. T. Mayer, C. Du, and D. Wang, *J. Am. Chem. Soc.*, **134**, 12406 (2012).
16. N. C. Strandwitz, D. J. Comstock, R. L. Grimm, A. C. Nichols-Nielander, J. Elam, and N. S. Lewis, *J. Phys. Chem. C*, **117**, 4931 (2013).
17. S. Hu, N. S. Lewis, J. W. Ager, J. Yang, J. R. McKone, and N. C. Strandwitz, *J. Phys. Chem. C*, **119**, 24201 (2015).
18. Y. W. Chen, J. D. Prange, S. Dühnen, Y. Park, M. Gunji, C. E. D. Chidsey, and P. C. McIntyre, *Nat. Mater.*, **10**, 539 (2011).
19. X. Ao, X. Tong, D. Sik Kim, L. Zhang, M. Knez, F. Müller, S. He, and V. Schmidt, *App. Phys. Lett.*, **101**, 111901 (2012).
20. Y. Lin, C. Battaglia, M. Boccard, M. Hettick, Z. Yu, C. Ballif, J. W. Ager, and A. Javey, *Nano Lett.*, **13**, 5615 (2013).
21. S. Hu, M. R. Shaner, J. A. Beardslee, M. Lichterman, B. S. Brunschwig, and N. S. Lewis, *Science*, **344**, 1005 (2014).
22. L. Santinacci, M. W. Diouf, M. K. S. Barr, B. Fabre, L. Joanny, F. Gouttefangeas, and G. Loget, *ACS Appl. Mater. Interfaces*, **8**, 24810 (2016).
23. M. Pavlenko, K. Siuzdak, E. Coy, M. Jancelewicz, S. Jurga, and I. Iatsunskyi, *Int. J. Hydrogen Energy*, **42**, 1 (2017).
24. V. S. Saji, *J. Electrochem. Soc.*, **167**, 121505 (2020).
25. Y. Wu, D. Döhler, M. Barr, E. Oks, M. Wolf, L. Santinacci, and J. Bachmann, *Nano Lett.*, **15**, 6379 (2015).
26. J.-P. Niemelä, G. Marin, and M. Karppinen, *Semicond. Sci. Technol.*, **32**, 093005 (2017).
27. M. E. Dufond, M. W. Diouf, C. Badie, C. Laffon, P. Parent, D. Ferry, D. Grosso, J. C. S. Kools, S. D. Elliott, and L. Santinacci, *Chem. Mater.*, **32**, 1393 (2020).
28. P. Schmuki, L. E. Erickson, and D. J. Lockwood, *Phys. Rev. Lett.*, **80**, 4060 (1998).
29. L. Santinacci, T. Djenizian, and P. Schmuki, *J. Electrochem. Soc.*, **148**, C640 (2001).
30. S. Hu, M. H. Richter, M. F. Lichterman, J. Beardslee, T. Mayer, B. S. Brunschwig, and N. S. Lewis, *J. Phys. Chem. C*, **120**, 3117 (2016).
31. P. Allongue, V. CostaKieling, and H. Gerischer, *J. Electrochem. Soc.*, **140**, 1009 (1993).
32. P. Allongue, V. Costa Kieling, and H. Gerischer, *J. Electrochem. Soc.*, **140**, 1018 (1993).
33. The anodic charge is calculated by integrating the current on the forward scan. The charge corresponding to the reverse scan and the small cathodic current at low potentials have not been deduced because they have a negligible impact on the value.
34. P. M. M. C. Bressers, S. A. S. P. Pagano, and J. J. Kelly, *J. Electroanal. Chem.*, **391**, 159 (1995).
35. O. J. Glembocki, *J. Electrochem. Soc.*, **132**, 145 (1985).
36. J. N. Chazalviel, *Electrochim. Acta*, **37**, 865 (1992).
37. X. H. Xia, C. M. A. Ashruf, P. J. French, J. Rappich, and J. J. Kelly, *J. Phys. Chem. B*, **105**, 5722 (2001).
38. H. G. G. Philipsen and J. J. Kelly, *J. Phys. Chem. B*, **109**, 17245 (2005).
39. H. G. G. Philipsen, F. Ozanam, P. Allongue, J. J. Kelly, and J. N. Chazalviel, *Surf. Sci.*, **644**, 180 (2016).

40. H. G. G. Philipsen, F. Ozanam, P. Allongue, J. J. Kelly, and J. N. Chazalviel, *J. Electrochem. Soc.*, **163**, H327 (2016).
41. X. H. Xia and J. J. Kelly, *Phys. Chem. Chem. Phys.*, **3**, 5304 (2001).
42. S. R. Morrison, *Electrochemistry at Semiconductor and Oxidized Metal Electrodes* (Plenum Press, New York) (1980).
43. N. Sbaï, J. Perrière, B. Gallas, E. Millon, W. Seiler, and M. C. Bernard, *J. Appl. Phys.*, **104**, 033529 (2008).
44. T. Berger, T. Lana-Villarreal, D. Monllor-Satoca, and R. Gómez, *Electrochemistry Communications*, **8**, 1713 (2006).
45. Q. Wang, Z. Zhang, S. M. Zakeeruddin, and M. Grätzel, *J. Phys. Chem. C*, **112**, 7084 (2008).
46. J. Idígoras, J. A. Anta, and T. Berger, *J. Phys. Chem. C*, **120**, 27882 (2016).
47. J. M. Jiménez, G. R. Bourret, T Berger, and K. P. McKenna, *J. Am. Chem. Soc.*, **138**, 15956 (2016).
48. C. K. Dyer and J. S. L. Leach, *J. Electrochem. Soc.*, **125**, 23 (1978).
49. K. C. Mandal, F. Ozanam, and J. N. Chazalviel, *Appl. Phys. Lett.*, **57**, 2788 (1990).
50. J. Idígoras, T. Berger, and J. A. Anta, *J. Phys. Chem. C*, **117**, 1561 (2013).
51. T. Berger, J. A. Anta, and V. Morales-Flórez, *J. Phys. Chem. C*, **116**, 11444 (2012).
52. T. Berger and J. A. Anta, *Anal. Chem.*, **84**, 3053 (2012).
53. J. Biedrzycki, S. Livraghi, E. Giamello, S. Agnoli, and G. Granozzi, *J. Phys. Chem. C*, **118**, 8462 (2014).
54. B. H. Meekins and P. V. Kamat, *ACS Nano*, **3**, 3437 (2009).
55. F. Giordano, A. Abate, J. P. C. Baena, M. Saliba, T. Matsui, S. H. Im, S. M. Zakeeruddin, M. K. Nazeeruddin, A. Hagfeldt, and M. Graetzel, *Nat. Commun.*, **7**, 10379 (2019).
56. G. Campet, C. Puprichitkun, and Z. W. Sun, *J. Electroanal. Chem. Interfacial Electrochem.*, **269**, 435 (1989).
57. H. J. Kim, K. L. Kearney, L. H. Le, Z. J. Haber, A. A. Rockett, and M. J. Rose, *J. Phys. Chem. C*, **120**, 25697 (2016).
58. X. Yao et al., *Applied Catalysis B: Environmental*, **221**, 70 (2018).
59. C. Di Valentin, G. Pacchioni, and A. Selloni, *J. Phys. Chem. C*, **113**, 20543 (2009).
60. M. F. Lichterman et al., *Energy Environ. Sci.*, **8**, 2409 (2015).
61. A. Márquez, M. J. Rodríguez-Pérez, J. A. Anta, G. Rodríguez-Gattorno, G. R. Bourret, G. Oskam, and T. Berger, *ChemElectroChem*, **3**, 658 (2016).